Remote Sensing of Environment 231 (2019) 111216

Contents lists available at ScienceDirect

Remote Sensing of Environment

journal homepage: www.elsevier.com/locate/rse

A new thermal infrared channel configuration for accurate land surface temperature retrieval from satellite data

Xiaopo Zheng[a], Zhao-Liang Li[a,b,*], Françoise Nerry[a], Xia Zhang[c]

[a] ICube Laboratory, UMR 7357, CNRS-University of Strasbourg, 300 bd Sébastien Brant, CS 10413, F-67412 Illkirch Cedex, France
[b] Key Laboratory of Agricultural Remote Sensing, Ministry of Agriculture/Institute of Agricultural Resources and Regional Planning, Chinese Academy of Agricultural Sciences, 100081 Beijing, China
[c] College of Land Resources and Urban and Rural Planning, Hebei GEO University, 050031 Shijiazhuang, China

ARTICLE INFO

Edited by Jing M. Chen

Keywords:
Thermal infrared data
Channel configuration
LST and LSE
Split window
Temperature-emissivity separation

ABSTRACT

Land surface temperature (LST) is an important parameter in many research fields. Many algorithms have been developed to retrieve LST from satellite thermal infrared (TIR) measurements; of these, the most widely used are the split window (SW) and temperature–emissivity separation (TES) methods. However, the performance of the SW and TES methods can be limited by the difficulty in obtaining sufficiently accurate prior knowledge—specifically, input land surface emissivity (LSE) for the SW method and atmospheric parameters for the TES method. In this study, a procedure was proposed for selecting specific channel pairs in the TIR spectral region to accurately retrieve ground brightness temperatures without prior atmospheric knowledge, using a method similar to the SW method. Subsequently, the TES method is applied to the retrieved ground brightness temperatures to separate the LST and LSE. In numerical simulations, the three ground brightness temperatures corresponding to 8.6 μm, 9.0 μm, and 10.4 μm are acquired with an accuracy of about 0.65 K by using five channels centered at 8.6 μm, 9.0 μm, 10.4 μm, 11.3 μm, and 12.5 μm, each with a width of 0.1 μm. When inputting the three retrieved ground brightness temperatures into TES method, LST could be recovered with an accuracy of 0.87 K. Sensitivity analysis shows that LST retrieval accuracy is less affected by channel width and atmospheric downwelling radiance than by the channel center locations and channel noise. Finally, the proposed method is preliminarily applied to actual satellite data from the Atmospheric InfraRed Sounder (AIRS) and the retrieved results are compared with the pixel-aggregated Moderate Resolution Imaging Spectroradiometer (MODIS) LST product. For the study area of Australia, discrepancies between our result and the MODIS LST product appear to be about 1.6 K during the day and 1.0 K at night, indicating that the new channel configuration can be used to retrieve accurate LST from satellite measurements.

1. Introduction

Land surface temperature (LST) is a key physical measurement of surface energy and water balance processes at both regional and global scales (Jackson et al., 1985; Jackson et al., 1977; Running et al., 1994; Sellers et al., 1988; Vining and Blad, 1992); it is used within many research fields, including hydrology, meteorology, and climatology (Anderson et al., 2008; Karnieli et al., 2010; Li et al., 2009; Tomlinson et al., 2011). Satellite remote sensing using measurements in the microwave (MW) and thermal infrared (TIR) spectral regions provides an efficient way to obtain the LST over extended regions (Becker and Li, 1990; Dash et al., 2001; Dash et al., 2002; Duan et al., 2017; McFarland et al., 1990; Schmugge et al., 1998; Yu et al., 2005). Although MW can penetrate through clouds, the resulting measurements have low spatial resolution and yield the "subsurface temperature" instead of the "skin temperature" provided by TIR remote sensing (Choudhury et al., 1982; Duan et al., 2017; Liu et al., 2013; Simmer, 1999). Furthermore, MW measurements are sensitive to soil moisture and surface roughness (Choudhury et al., 1979; Njoku and Entekhabi, 1996). Because of these shortcomings, TIR measurements are more widely used than MW measurements for LST retrieval. However, to determine an accurate LST, the data from satellite TIR measurements must be corrected for the effects of atmosphere and land surface emissivity (LSE) (Becker, 1987; Sobrino et al., 1991). In recent decades, many algorithms have been developed for this purpose (Dash et al., 2002; Li et al., 2013a; Prata et al., 1995; Sattari and Hashim, 2014); they can be roughly classified into four types (Li et al., 2013a; Li et al., 2013b): the single-channel (Jimenez-Munoz and Sobrino, 2003; Ottle and Vidalmadjar, 1992; Qin

* Corresponding author at: ICube Laboratory, UMR 7357, CNRS-University of Strasbourg, 300 bd Sébastien Brant, CS 10413, F-67412 Illkirch Cedex, France.
E-mail address: lizl@unistra.fr (Z.-L. Li).

https://doi.org/10.1016/j.rse.2019.111216
Received 29 October 2018; Received in revised form 19 April 2019; Accepted 25 May 2019

et al., 2001a), day/night (Wan, 2008; Wan, 2014; Wan and Li, 1997; Wan and Li, 2008), split window (SW) (Becker and Li, 1990; Coll and Caselles, 1997; McMillin, 1975; Qin et al., 2001b; Wan and Dozier, 1996), and temperature-emissivity separation (TES) (Gillespie et al., 1998) methods. With the use of these methods, LSTs have been successfully retrieved from satellite measurements under specific assumptions.

As documented in previous studies (Li et al., 2013a; Li et al., 2013b; Sattari and Hashim, 2014), these commonly used methods have advantages as well as disadvantages. The single channel method utilizes a simple inversion of the radiative transfer equation and requires accurate LSE and atmospheric profiles in order to provide accurate LST retrievals (Ottle and Vidalmadjar, 1992). In comparison, the day/night method only needs the shape information of the atmospheric profiles and can retrieve the LST and LSE simultaneously; however, large errors may be introduced into the retrieved results if the temporal images are geometrically misregistered or the LSE changes significantly from day to night (Wan and Li, 1997). In addition, the complexity of the equation-solving task also limits this method's application. Alternatively, the SW method can accurately eliminate atmospheric effects by combining measurements from two adjacent channels. This method represents the LST as a polynomial function of the two channel brightness temperatures and is easy to apply; however, LSEs of the two channels must be known accurately to provide good LST retrievals (Becker, 1987). The TES method can also separate the LST and LSE simultaneously, although it requires accurate ground brightness temperatures as input, meaning that the performance of the TES method is dependent on the accuracy of atmospheric correction (Gillespie et al., 1998). Each of these existing methods has limitations and may be unable to meet the LST retrieval accuracy of ≤ 1.0 K that is required by many disciplines under certain circumstances (Sobrino et al., 2016). Considering the complementary advantages and disadvantages of the SW and TES methods, a hybrid method was proposed by Ren et al. (2018) to improve LST retrieval accuracy. That being said, the improvements are questionable because this method still does not address the accurate atmospheric correction required by the TES algorithm. To overcome this problem, this study proposes a procedure to select specific channel pairs in the TIR spectral region for retrieving accurate ground brightness temperatures from satellite observations by using a method that is similar to the SW method. When applying the TES method to these retrieved ground brightness temperatures, the LST can be accurately retrieved without any prior LSE or atmospheric knowledge.

This paper is organized as follows: Section 2 demonstrates the theoretical basis of the proposed method; Section 3 describes the method for determining the new channel configuration; Section 4 presents a sensitivity analysis of the proposed method; and Section 5 covers a preliminary application and validation with real satellite data. Finally, Section 6 summarizes our main findings.

2. Methodology

Drawing on the SW method, a procedure was deduced for acquiring accurate ground brightness temperatures. The general radiative transfer equation for TIR remote sensing can be formulated as follows (Becker and Li, 1990; Wan and Dozier, 1996; Wan and Li, 1997):

$$B(T_i) = \tau_i B(T_{gi}) + L_i^{\uparrow}, \tag{1}$$

with

$$B(T_{gi}) = \varepsilon_i B(T_s) + (1 - \varepsilon_i) L_i^{\downarrow}, \tag{2}$$

where subscript i is channel i; T_i and T_{gi} are the brightness temperature and ground brightness temperature of channel i, respectively; B represents the Planck function; ε_i and T_s are the LSE and LST; τ_i denotes the atmospheric transmittance of channel i; and $L_i^{\downarrow}$ and $L_i^{\uparrow}$ are the atmospheric downwelling and upwelling radiance of channel i. When employing the mean value theorem (Coll et al., 1994; McMillin, 1975; Prata, 1993), $L_i^{\uparrow}$ can be expressed by

$$L_i^{\uparrow} = (1 - \tau_i) B(T_{ai}), \tag{3}$$

where T_{ai} is the effective mean atmospheric temperature. Substituting Eq. (3) into Eq. (1) produces

$$B(T_i) = \tau_i B(T_{gi}) + (1 - \tau_i) B(T_{ai}). \tag{4}$$

Eq. (4) can also be applied to another channel, j:

$$B(T_j) = \tau_j B(T_{gj}) + (1 - \tau_j) B(T_{aj}). \tag{5}$$

Assuming that the ground brightness temperature, effective mean atmospheric temperature, and brightness temperature of channels i and j are close to each other, the first-order Taylor series of the Planck function can be applied to Eq. (4) and Eq. (5) around T_i, as follows:

$$T_i - T_{ai} = \tau_i (T_{gi} - T_{ai}) \tag{6}$$

$$T_j - T_{aj} = \tau_j (T_{gj} - T_{aj}). \tag{7}$$

T_{ai} can be expressed as a linear function of T_{aj},

$$T_{ai} = m T_{aj} + n, \tag{8}$$

where m and n are constants related to channels. By combining Eq. (6), Eq. (7), and Eq. (8), and eliminating T_{ai} and T_{aj}, T_{gi} could be written as a function of T_i and T_j, as in the SW method:

$$T_{gi} = k + p T_i + q (T_i - T_j) + \Delta, \tag{9}$$

with

$$k = \frac{n(\tau_i - 1)(\tau_j - 1)}{m\tau_j(1 - \tau_i) - \tau_i(1 - \tau_j)} \tag{10}$$

$$p = \frac{(\tau_j - 1) - m(\tau_i - 1)}{m\tau_j(1 - \tau_i) - \tau_i(1 - \tau_j)} \tag{11}$$

$$q = \frac{(\tau_i - 1)}{m\tau_j(1 - \tau_i) - \tau_i(1 - \tau_j)} \tag{12}$$

$$\Delta = \frac{m\tau_j(\tau_i - 1)}{m\tau_j(1 - \tau_i) - \tau_i(1 - \tau_j)} (T_{gj} - T_{gi}). \tag{13}$$

When the atmospheres are not too wet, the coefficients of k, p and q can be considered as constants. If the channel combination of i and j meets at least one of these conditions for different atmospheres and land surfaces—(1) Δ is close to zero, (2) Δ is a linear function of T_i, or (3) Δ is a linear or quadratic function of $(T_i - T_j)$—then T_{gi} can be directly retrieved from satellite measurements, as with the SW method for the sea surface [Eq. (14)]:

$$T_{gi} = A_0 + A_1 T_i + A_2 (T_i - T_j) + A_3 (T_i - T_j)^2, \tag{14}$$

where A_0, A_1, A_2, and A_3 are constants. The introduction of the quadratic item $A_3(T_i - T_j)^2$ further improves the retrieval accuracy of T_{gi}, as in the SW method (Coll and Caselles, 1997; Coll et al., 1994; Du et al., 2015; Galve et al., 2008; Sobrino et al., 1993; Wan, 2014).

After obtaining accurate T_{gi}, the TES method can be applied to retrieve the LST with high accuracy. Because the TES method requires at least three T_{gi} as inputs (Sobrino and Jiménez-Muñoz, 2014), it is critical to find a minimum of three channel pairs that can be applied to Eq. (14) to obtain at least three accurate T_{gi} in the TIR region. Subsequently, the LST can be accurately retrieved using the TES algorithm, provided that the spectral locations of T_{gi} provide a good empirical relationship between the minimum emissivity (ε_{min}) and maximum–minimum emissivity difference (*MMD*) (Gillespie et al., 1998; Hu et al., 2015). An illustration of the proposed method is shown in Fig. 1.

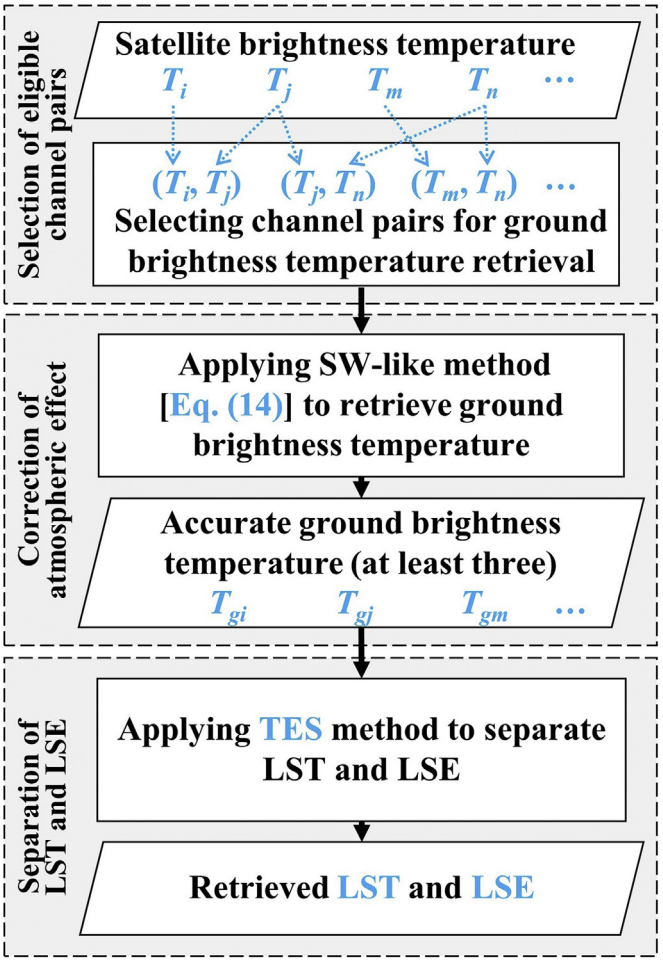

Fig. 1. Illustration of the proposed method for accurate LST retrieval.

3. Determination of the new channel configuration

Because the commonly used TIR images do not provide the channel pairs required by the method described in Section 2, a new channel configuration needs to be determined. First, a simulation dataset was made using the MODerate resolution atmospheric TRANsmission (MODTRAN) code (Berk et al., 2005). Then, channel pairs that were eligible to retrieve accurate T_{gi} using Eq. (14) were searched iteratively in the TIR region with the help of the simulation dataset. Finally, the spectral locations of the eligible channels were optimized manually. A detailed flow diagram of this process is shown in Fig. 2.

3.1. Simulation dataset for determining a new channel configuration

By using MODTRAN, the satellite channel brightness temperatures in the TIR region can be simulated given the LSE, LST, atmosphere profiles, and channel filter functions. As in the method suggested by (Sobrino and Jiménez-Muñoz, 2014), the channel filter function was simulated as a composite form of the Gaussian and triangle functions. The equations can be expressed as

$$f(\lambda) = \begin{cases} \dfrac{\lambda}{FWHM} + \left(1 - \dfrac{\lambda_0}{FWHM}\right)\lambda_0 - FWHM < \lambda < \lambda_0 - \dfrac{FWHM}{2} \\ \exp\left[-\dfrac{(\lambda - \lambda_0)^2}{2\sigma^2}\right] \lambda_0 - \dfrac{FWHM}{2} < \lambda < \lambda_0 + \dfrac{FWHM}{2} \\ -\dfrac{\lambda}{FWHM} + \left(1 + \dfrac{\lambda_0}{FWHM}\right)\lambda_0 + \dfrac{FWHM}{2} < \lambda < \lambda_0 + FWHM \end{cases} \quad (15)$$

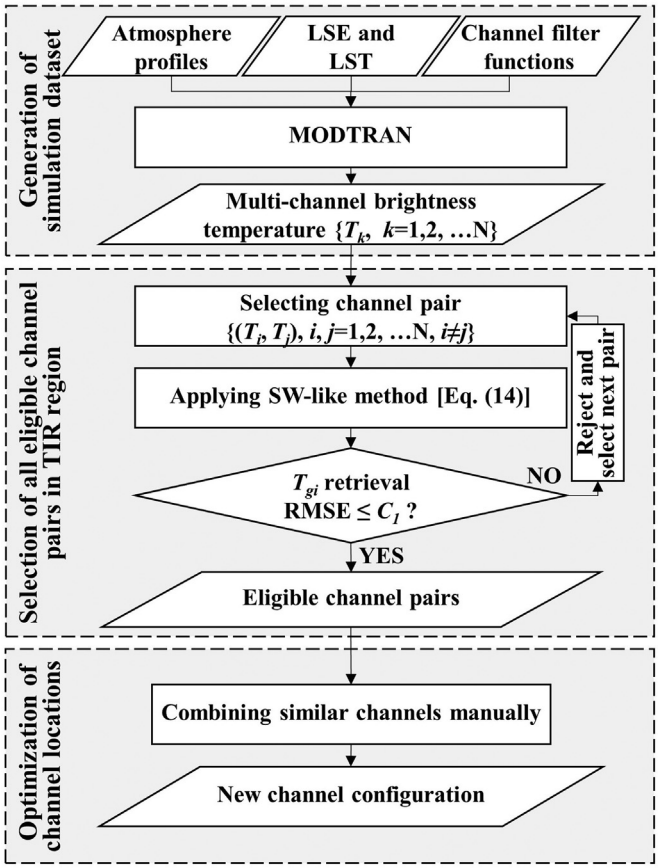

Fig. 2. Flow diagram for determining the new channel configuration. T_k, T_i, and T_j are channel brightness temperatures, C_1 is a constant for testing whether a channel pair is eligible to retrieve accurate ground brightness temperature.

where $f(\lambda)$ is the channel filter function; λ is the wavelength; *FWHM*, the full width at half maximum, is the channel width; λ_0 is the channel center; and σ is the width of the Gaussian function, which is related to the *FWHM* by $\sigma = FWHM/(2\sqrt{2\ln 2}) \approx 0.42FWHM$. In this study, the spectral region from 8.0 μm to 14.0 μm was considered, with channel center intervals of 0.1 μm. The *FWHM* of each channel was initially set as 0.1 μm. Thus, 59 successive channel filter functions were generated using Eq. (15) (Fig. 3).

Following the research of Chen et al. (2017), 65 LSE spectra were selected from the ECOSTRESS Spectral Library, Version 1.0 (https://speclib.jpl.nasa.gov/) to represent different land surface coverages, including 52 soil, 4 vegetation, and 9 water/ice/snow samples (Fig. 4a, b, and c). Additionally, 98 atmosphere profiles were selected from the Thermodynamic Initial Guess Retrieval (TIGR, http://ara.abct.lmd.polytechnique.fr/) database, with the water vaper content ranging

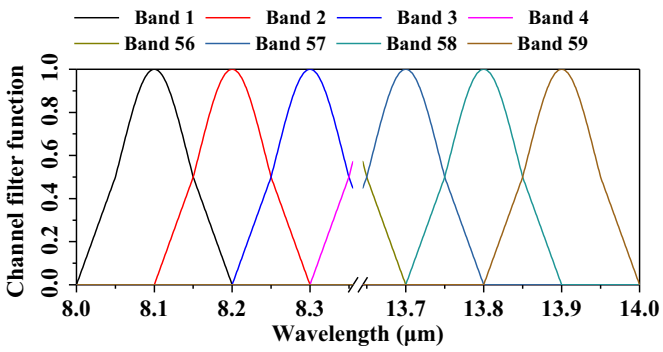

Fig. 3. Simulated channel filter functions.

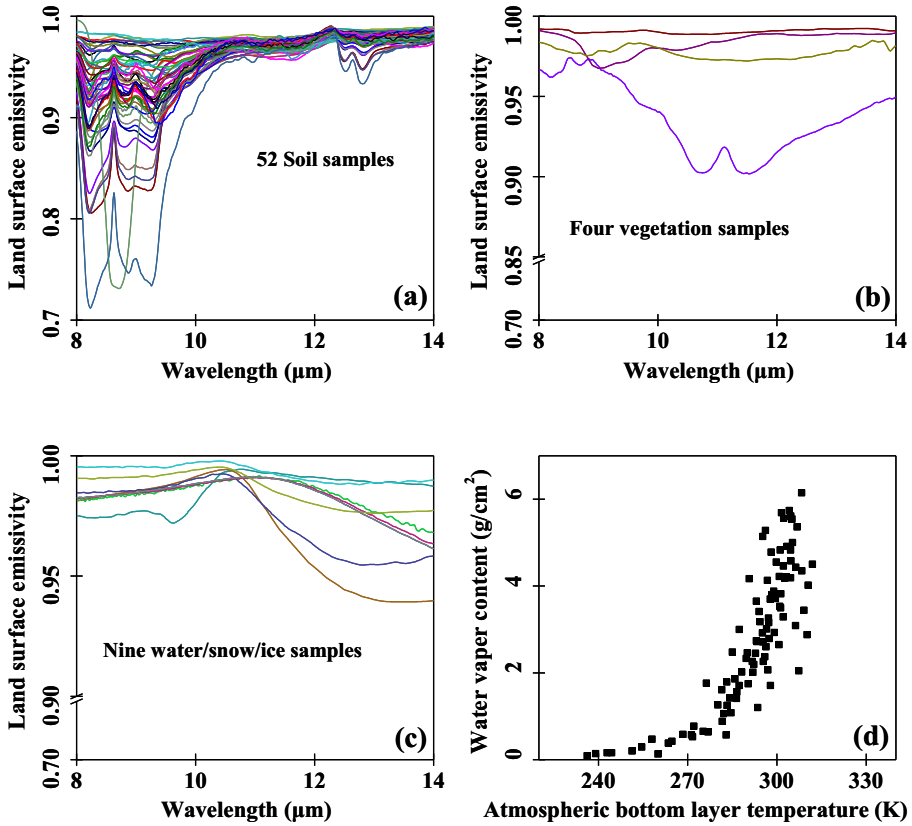

Fig. 4. (a) LSE spectra of the 52 soil samples, (b) LSE spectra of the four vegetation samples, (c) LSE spectra of the nine water/snow/ice samples, and (d) scatter plot of the bottom layer temperature and water vaper content of the 98 atmosphere profiles.

from 0.09 g/cm^2 to 6.15 g/cm^2. The input LST was assigned according to the bottom layer temperature T_0 of each atmosphere profile. If $T_0 \geq 280$ K, then the LST varied from T_0–5 K to T_0 + 15 K with intervals of 5 K. Otherwise, the LST varied from T_0–5 K to T_0 + 5 K with intervals of 5 K (Chen et al., 2017). With the input parameters described above, 29,640 cases were generated in the simulation dataset.

3.2. Selection of eligible channel pairs for retrieving ground brightness temperature

Theoretically, there are 3363 possible two-channel combinations using the 59 simulated channels, although some of them do not meet the conditions that eligible channel pairs conform to; that is, the value of Δ in Eq. (9) is neither close to zero, nor a linear function of T_i, nor a linear or quadratic function of $(T_i - T_j)$. In this study, the root-mean-square error (RMSE) of the retrieved T_{gi} was chosen as an indicator of whether a channel pair met at least one of these conditions. A threshold (i.e., C_1 in Fig. 2) of 0.7 K was used to find all eligible channel pairs. This threshold was determined by trial-and-error to allow the final LST to be retrieved within the expected accuracy of 1.0 K. After filtering by the threshold and excluding channels inside the ozone absorption band from 9.4 μm to 10.0 μm, 44 eligible channel pairs associated with 28 individual channels remained (Fig. 5).

3.3. Optimization of eligible channel locations

Some of the 28 channels composing the 44 remaining eligible channel pairs from Section 3.2 were very similar, as a result of the channel filter functions being generated with a small channel center interval of 0.1 μm. Thus, it was reasonable to reduce the total number of channels; specifically, some channels were removed so that adjacent channel center intervals were greater than or equal to 0.2 μm. This process was done manually in order to evenly distribute the locations of the remaining channels. After refinement, 16 of the 28 individual channels remained (marked by triangles in Fig. 6a), forming 18 eligible channel pairs (Fig. 6b).

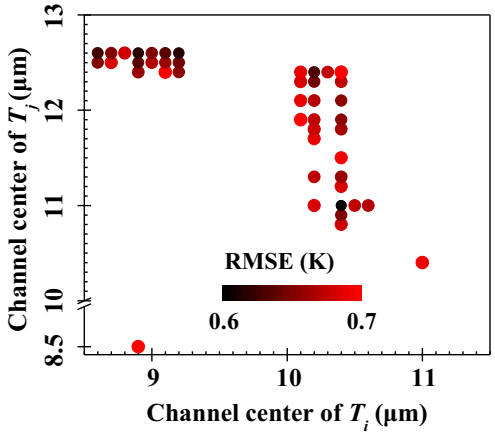

Fig. 5. The spectral centers of eligible channel pairs. The retrieval RMSE of the ground brightness temperature of channel i (T_{gi}) is represented by the color scale.

3.4. Retrieval of ground brightness temperature and LST

Using the refined eligible channel pairs, seven highly accurate T_{gi} were retrieved. Note that the T_{gi} at 10.2 μm and 10.4 μm could be retrieved repeatedly by combining with different T_j (Fig. 6b). Therefore, the retrieved T_{gi} of the channels at 10.2 μm and 10.4 μm were averaged respectively before applying the TES algorithm. Numerical simulations

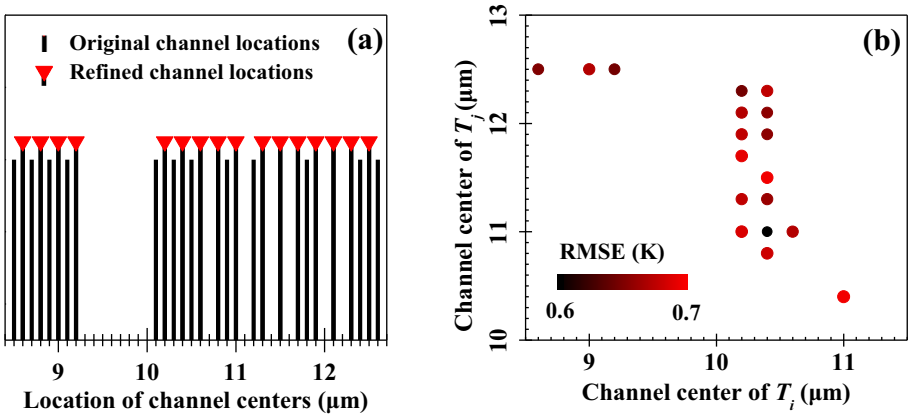

Fig. 6. Optimization of the eligible channel locations. (a) Channels remaining after refinement are indicated by triangles; (b) eligible channel pairs remaining after refinement for retrieving the ground brightness temperature of channel i (T_{gi}).

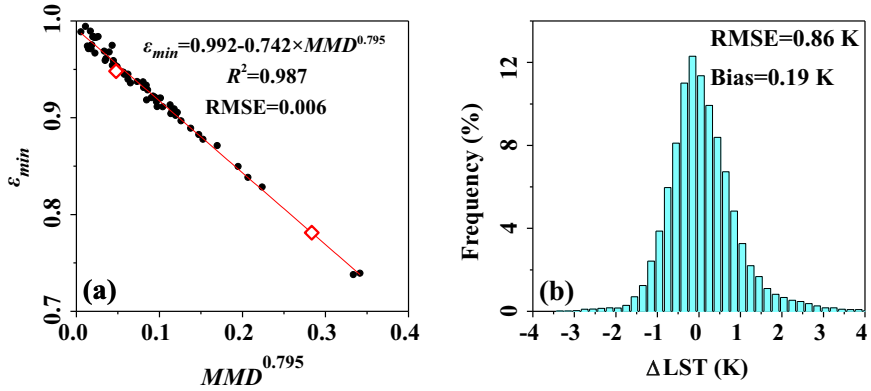

Fig. 7. (a) The empirical relationship between ε_{min} and MMD, based on the 65 samples described in Section 3.1. Diamonds represent two additional rock samples used in Section 4.3 for sensitivity analysis. (b) Histogram of the residuals between the retrieved and true LSTs.

indicated that the spectral locations of T_{gi} provided a good $\varepsilon_{min} \sim MMD$ relationship (Fig. 7a) and LST could be retrieved to within 1.0 K by using the refined eligible channels (Fig. 7b).

Previous studies indicated that three T_{gi} can meet the minimum requirement of the TES algorithm (Gillespie et al., 1998; Sobrino and Jiménez-Muñoz, 2014). Considering 16 individual channels connected with the 18 remaining eligible channel pairs is unreasonable when developing an instrument; therefore, only three eligible channel pairs were selected to study the performance of the proposed method. To accurately retrieve the LST, the spectral locations of the T_{gi} should provide enough emissivity contrast to estimate the ε_{min}. Detailed information about the three channel pairs used in this study is listed in Table 1. Retrieval results indicated that the T_{gi} at 8.6 μm, 9.0 μm, and 10.4 μm could be acquired with accuracies of approximately 0.65 K using Eq. (14) (Fig. 8a), and showed that the LST could be retrieved with an accuracy of ≤ 1.0 K using these three T_{gi} (Fig. 8b). Therefore, in the following sections, a configuration of 8.6 μm, 9.0 μm, 10.4 μm, 11.3 μm, and 12.5 μm for the five channels was used as an example, although other appropriate options may also exist.

Table 1
The three recommended channel pairs for retrieving T_{gi} and the fitted coefficients of Eq. (14).

Center of channel i (μm)	Center of channel j (μm)	A_0	A_1	A_2	A_3	T_{gi} retrieval RMSE (K)
8.6	12.5	−6.75	1.03	0.39	0.02	0.64
9.0	12.5	−3.79	1.02	0.30	0.02	0.66
10.4	11.3	0.27	1.00	1.04	0.20	0.65

4. Sensitivity analysis

4.1. Sensitivity analysis to channel noise and channel width

4.1.1. Sensitivity analysis to channel noise with a channel width of 0.1 μm

Instrumental noise causes actual observed channel brightness temperatures to contain random errors that could affect LST retrieval accuracy. Therefore, a sensitivity analysis was performed by adding a noise-equivalent differential temperature (NEΔT) to the simulated channel brightness temperatures before applying the proposed method. The results showed that the RMSEs of the three retrieved T_{gi} increased with the channel NEΔTs, and the channel at 10.4 μm was more sensitive to channel noise than the other two channels (Fig. 9a). The biases of the retrieved LST indicated that the results were overestimated; this is believed to be caused by the introduction of the quadratic item in Eq. (14) (Fig. 9b). Results also showed that the RMSE of the retrieved LST slightly increased, but was still accurate to within 1.0 K, when the NEΔT was below 0.1 K; however, accuracy was only within 1.2 K and 1.4 K when noise levels of 0.2 K and 0.3 K, respectively, were added to the channel brightness temperatures (Fig. 9b). Therefore, channel noise must be well controlled to accurately retrieve LSTs using the proposed method.

4.1.2. Sensitivity analysis to channel width without channel noise

The retrieval accuracies of T_{gi} and LST may also affected by the channel witdth. To evaluate the impact of this factor, a sensitivity analysis was performed by varying the channel FWHM before obtaining the simulated channel brightness temperatures. As the channels broadened, the retrieval accuracy of the T_{gi} at 8.6 μm rapidly decreased

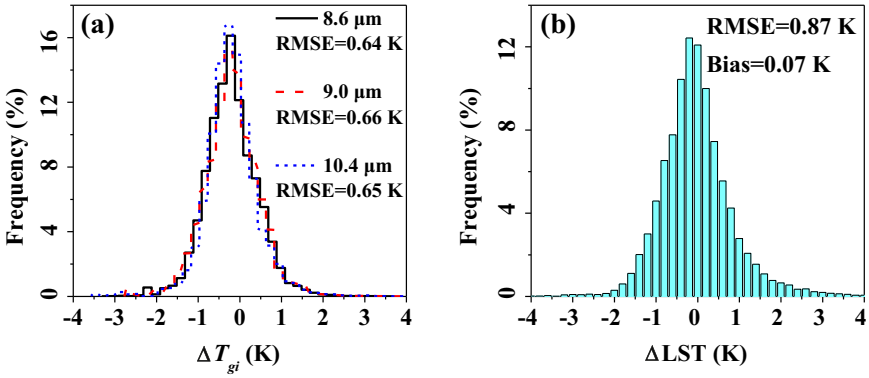

Fig. 8. (a) Histograms of the residuals between the retrieved and true ground brightness temperature (T_{gi}) for different channels. (b) Histogram of the residuals between the retrieved and true LST.

(Fig. 10a). Although the RMSEs of the other two channels also generally increased with the FWHM (Fig. 10a), they were less affected when the channel FWHM was in some certain ranges (0.1–0.4 μm for the channel at 9.0 μm and 0.3–0.5 μm for the channel at 10.4 μm). Additionally, LST retrieval accuracy decreased to about 1.0 K as the FWHM increased to 0.3 μm, whereas the RMSE of the retrieved LST only slightly increased as channel width continuously increased (Fig. 10b); this variation pattern was similar to that for the retrieval accuracy of T_{gi} at 10.4 μm. This may have occurred because, in the TES algorithm, LST is always calculated from the channel with the highest emissivity. For most land surface coverages, the emissivity of the channel at 10.4 μm is larger than that of the other two channels. Thus, LST retrieval accuracy was more influenced by the T_{gi} retrieval accuracy for the channel at 10.4 μm.

4.1.3. Sensitivity analysis to channel width with channel noise

Since channel noise is related to channel width, the accuracy of retrieved LST for different combinations of channel NEΔT and channel FWHM was also analyzed. The results showed that the RMSE of the retrieved LST increased with FWHM up to 0.3 μm and then stabilized (Fig. 11). A maximum error of about 0.3 K was introduced to LST retrievals as the channel width was broadened from 0.1 μm to 0.6 μm. Furthermore, LST retrieval accuracy was more influenced by the channel noise because the NEΔT was magnified twice and transferred to the final LST retrievals (Fig. 11). As shown in Fig. 11, when both factors are considered, the LST should be retrieved within the accuracy of about 1.2 K and 1.5 K for sensors with a channel NEΔT of 0.1 K and 0.2 K, respectively.

4.2. Sensitivity analysis to the channel center

For actual satellite instruments, the channel filter functions are not ideal mathematical functions (in contrast with the Gaussian and triangle functions used in Section 3.1), which may lead to the shift of effective channel centers. Therefore, impact of channel-center shifts on LST retrieval accuracy using the proposed method was evaluated. Offsets of −0.2 μm to 0.2 μm, with intervals of 0.1 μm, were added to the spectral centers of the five channel filter functions before simulating the satellite brightness temperatures. For simplicity, the same offset value was used for all five involved channels each time. The results showed that the retrieval accuracies of T_{gi} at 8.6 μm and 10.4 μm decreased along with the shifting of channel centers. Additionally, these two T_{gi} were retrieved less accurately when the channel centers shifted to shorter wavelengths than when they shifted to longer wavelengths (Fig. 12a). The retrieval accuracy of T_{gi} at 9.0 μm was unaffected by channel-center shifts, except for those of −0.2 μm (Fig. 12a). With the shifting of channel centers, retrieved LSTs were overestimated and retrieval accuracy decreased to > 1.0 K (Fig. 12b). These results indicate that a shift of channel centers introduces large errors to the retrieved T_{gi} and LST. Therefore, it is highly recommended to keep the channel centers at their initial locations when possible.

4.3. Sensitivity analysis to atmospheric downwelling radiance and LSE characteristics

The original TES algorithm requires the atmospheric downwelling radiance in order to refine the retrieved LST and LSE. The above results are all based on the simulated atmospheric downwelling radiance of the three selected channels ($L_{8.6\ \mu m}^{\downarrow}$, $L_{9.0\ \mu m}^{\downarrow}$, and $L_{10.4\ \mu m}^{\downarrow}$) without uncertainties. Therefore, it is necessary to investigate the influence on LST

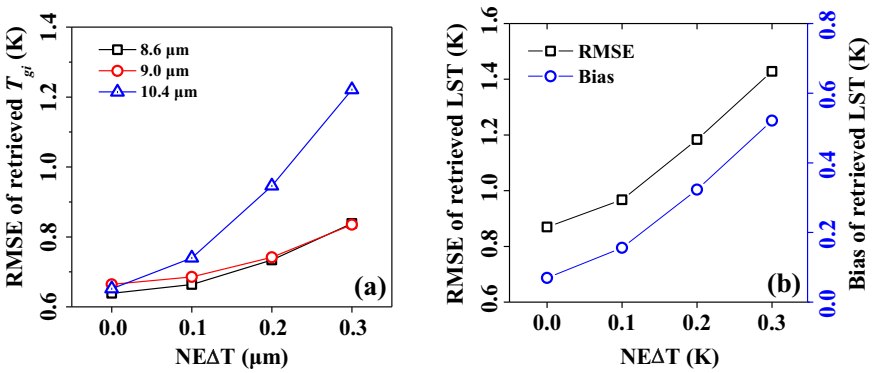

Fig. 9. (a) The RMSEs of the retrieved ground brightness temperatures for different channels (T_{gi}) as a function of channel NEΔT. The channel FWHM was fixed at 0.1 μm. (b) The LST retrieval RMSE and bias as a function of channel NEΔT.

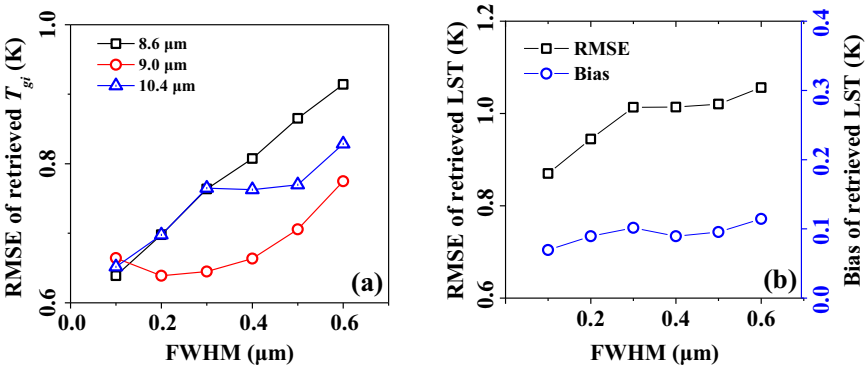

Fig. 10. (a) The RMSE of retrieved ground brightness temperature for different channels (T_{gi}) as a function of channel FWHM. The channel NEΔT was fixed at 0.0 K. (b) The LST retrieval RMSE and bias as a function of channel FWHM.

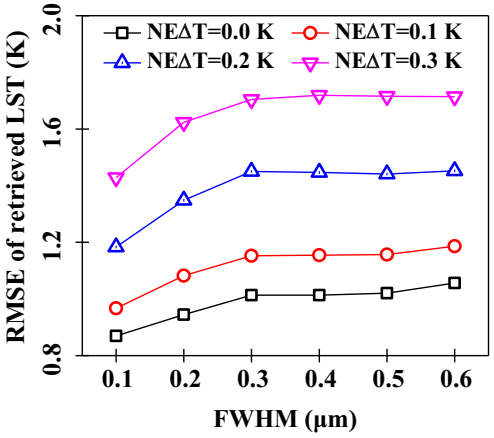

Fig. 11. The LST retrieval RMSE as a function of channel FWHM for different levels of channel NEΔTs.

retrieval accuracy when real atmospheric measurements, or products containing errors, are used. In this study, sensitivity analysis was conducted by adding relative errors to $L_{8.6\ \mu m}^{\downarrow}$, $L_{9.0\ \mu m}^{\downarrow}$, and $L_{10.4\ \mu m}^{\downarrow}$ before applying the TES algorithm. Since $L_{8.6\ \mu m}^{\downarrow}$, $L_{9.0\ \mu m}^{\downarrow}$, and $L_{10.4\ \mu m}^{\downarrow}$ are highly correlated with each other, the empirical relationships between $L_{9.0\ \mu m}^{\downarrow}$ and $L_{8.6\ \mu m}^{\downarrow}$, and between $L_{10.4\ \mu m}^{\downarrow}$ and $L_{8.6\ \mu m}^{\downarrow}$ were first built using quadratic functions with an intercept of zero (Fig. 13a). Then, relative errors from −40% to 40%, with intervals of 10%, were added to $L_{8.6\ \mu m}^{\downarrow}$. Using the two empirical relationships shown in Fig. 13a, $L_{9.0\ \mu m}^{\downarrow}$ and $L_{10.4\ \mu m}^{\downarrow}$ with relative errors could also be acquired. Subsequently, the LST was retrieved using these inaccurate atmospheric downwelling radiance measurements instead of the simulations without uncertainties.

Results showed that the RMSE of the retrieved LSTs increased as relative errors were introduced into the atmospheric downwelling radiance (Fig. 13b). Overestimation of the atmospheric downwelling radiance had slightly a larger influence on LST retrieval accuracy than underestimation. However, the LST retrieval results were still acceptable, with an RMSE < 1.0 K, even when a relative error of 40% was added to the atmospheric downwelling radiance (Fig. 13b). One possible reason for this phenomenon is that the final LST is always calculated from the channel with the largest emissivity in the TES algorithm (Gillespie et al., 1998).

Previous studies (Gillespie et al., 1999; Jimenez-Munoz et al., 2014) have also shown that errors in estimating atmospheric downwelling radiance are of minor significance for LST retrieval in most situations when using the TES algorithm. However, for warm atmospheres over cold and highly reflective ground surfaces, such errors may become significant enough to limit the TES algorithm's performance (Gillespie et al., 1998). In fact, the impact of inaccurate atmospheric downwelling radiance to the TES is complicated because the reflected atmospheric downwelling radiance is corrected based on the estimated emissivity, which may already be in error (Gustafson et al., 2006). To investigate the impact of these two coupled error sources on LST retrieval accuracy, biases were added to both the atmospheric downwelling radiance and ε_{min}. Considering that ε_{min} can be obtained with an uncertainty of about 0.006, using its relationship with *MMD* as illustrated in Fig. 7a, a value of 0.015 was used as the maximum bias introduced to ε_{min}. The maximum bias used for the atmospheric downwelling radiance was 40%. As shown in Fig. 13c, the impact of inaccurate atmospheric downwelling radiance on LST retrieval accuracy depends on the emissivity error. For cases in which these two source errors have opposite signs, their impact on the retrieved LST is reduced; otherwise, it is amplified. We also found that the LST could be retrieved with an accuracy of 1.0 K for most cases in which the uncertainty in the estimated ε_{min} was < 0.0075. To

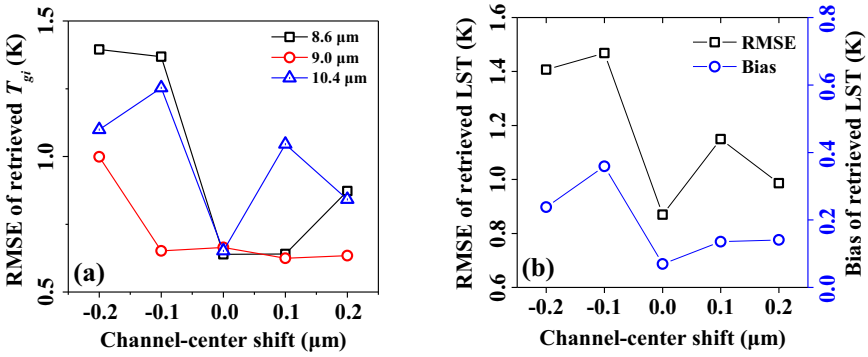

Fig. 12. (a) The RMSE of retrieved ground brightness temperature for different channels (T_{gi}) as a function of channel-center shifts. (b) The LST retrieval RMSE and bias as a function of channel-center shifts.

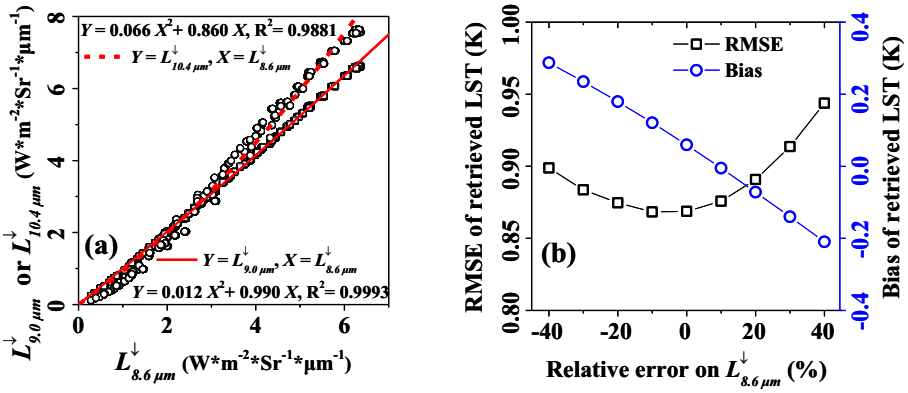

Fig. 13. (a) The empirical relationships between $L_{9.0\ \mu m}{}^{\downarrow}$ and $L_{8.6\ \mu m}{}^{\downarrow}$, and $L_{10.4\ \mu m}{}^{\downarrow}$ and $L_{8.6\ \mu m}{}^{\downarrow}$. (b) The LST retrieval RMSE and bias as a function of relative errors on the atmospheric downwelling radiance. (c) RMSE of retrieved LST using our proposed method with errors in both atmospheric downwelling radiance and minimum emissivity (ε_{min}).

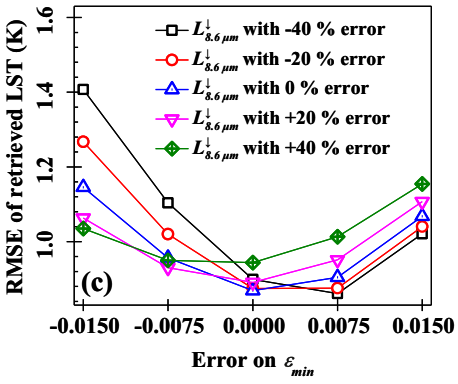

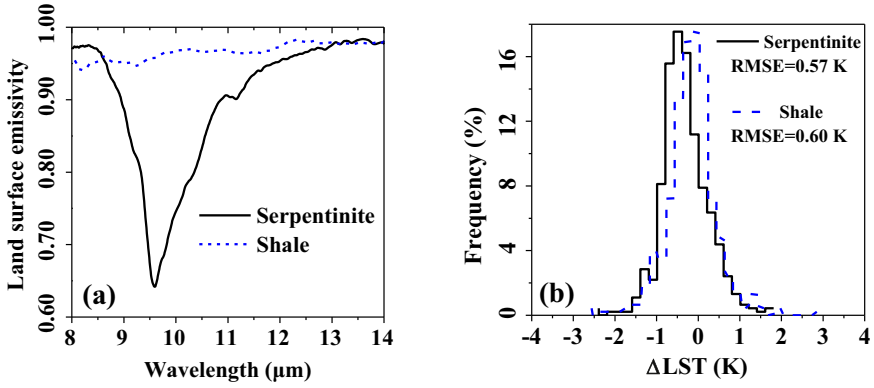

Fig. 14. (a) Additional LSE spectra, of two rocks, with different shapes from the previous 65 LSE samples displayed in Fig. 4. (b) Histogram of the residuals between the LST retrieved using the proposed method from data simulated with the spectra given in (a) and the true LST.

illustrate the impact of surface emissivity characteristics on the retrieved LST, two additional LSE spectra (Fig. 14a) with different shapes from the previous 65 LSE samples (Fig. 4) were used. As shown in Fig. 7a (the diamond symbols), although the two LSE spectra are different from the 65 LSE spectra used in Section 3, provided that the surface spectra follow the $\varepsilon_{min} \sim MMD$ relationship, the LST for these two rocks can be retrieved using our proposed method with an accuracy better than 0.6 K (Fig. 14b).

5. Application

The proposed method and suggested channel configuration were also applied to real satellite data to preliminarily verify its accuracy. Because no existing sensors have such a channel configuration, the level 1C hyper-spectral radiance of the Atmospheric InfraRed Sounder (AIRS_L1C) was introduced to calculate the theoretical measurements of the five required broad channels by using simulated channel filter functions (Moustafa, 2015). The pixel size of the AIRS image is 13.5 km × 13.5 km at nadir and is difficult to patch with ground truth measurements. Therefore, retrieval results were validated by comparison with the Land Surface Temperature/Emissivity 5-Min L2 Swath 1 km product (MYD11_L2) acquired by the Moderate Resolution Imaging Spectroradiometer (MODIS) (Wan et al., 2015). A detailed processing flow diagram is shown in Fig. 15.

In one process, the LST was retrieved by using the proposed method on the theoretical multichannel observations acquired from AIRS hyper-spectral radiance. As demonstrated in Section 4.3, the impact of atmospheric downwelling radiance on the retrieved LST is small. Therefore, in this study, the required atmospheric downwelling radiance was estimated using MODTRAN with an atmospheric profile selected from the five standard profiles (Tropical, Mid-Latitude Summer, Mid-Latitude Winter, Sub-Arctic Summer, Sub-Arctic Winter)

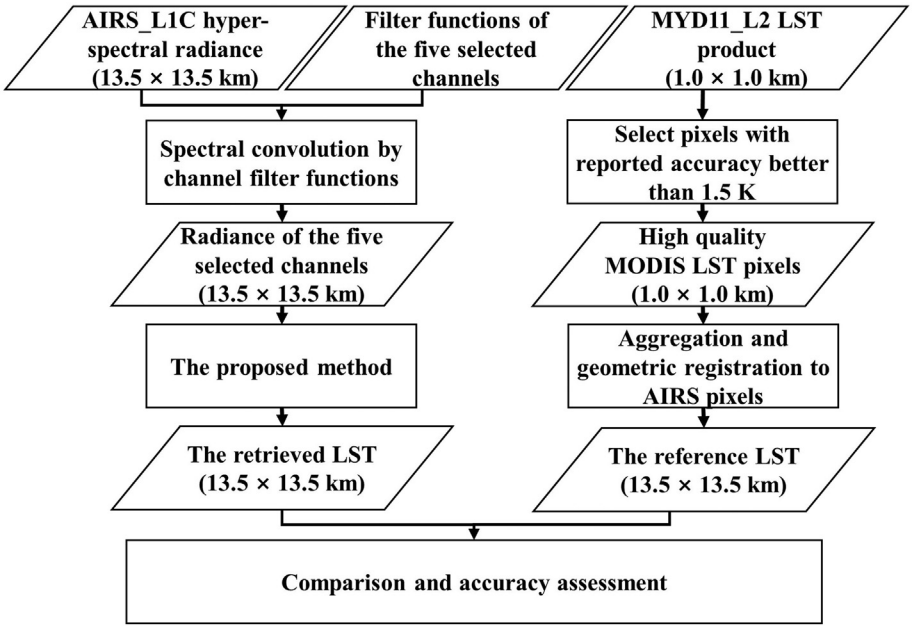

Fig. 15. The flow diagram of application based on real satellite data.

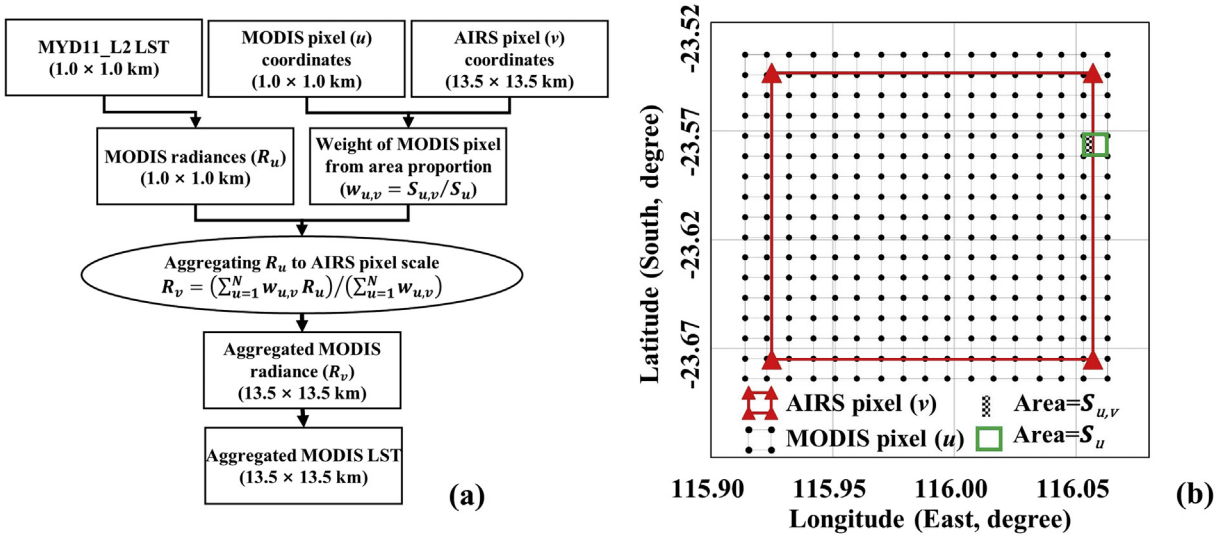

Fig. 16. (a) Flow diagram of the MODIS LST aggregating process, where N is the total number of MODIS pixels u inside or overlapped by one AIRS pixel v. (b) Illustration of the relationship between AIRS and MODIS pixel coordinates, where $S_{u,v}$ is the area of overlap between pixels u and v and S_u is the total area of pixel u.

using the method proposed by Harris (2009, Table 2-2) with the data acquisition month and the pixel geolocation (latitude). In another process, the MODIS LST product (MYD11_L2) was aggregated to match the AIRS spatial resolution for comparison using the area-weighted pixel aggregation algorithm (Gao et al., 2012; Qian et al., 2013). Detailed procedures are shown in Fig. 16. First, the MODIS LSTs were converted to radiance. Then, the weight of each MODIS pixel was calculated from the relationships between MODIS and AIRS pixel coordinates. Next, the radiance of all MODIS pixels inside or overlapped by the AIRS pixel were weighted to obtain the aggregated MODIS radiance with the spatial size of AIRS pixel. Finally, the aggregated MODIS LST was calculated from the aggregated radiance using the inverted Planck function.

Note that four restrictions were applied to refine the validation pixels. First, the "Error_LST" layer in the MYD11_L2 product was used to select cloud-free MODIS pixels that did not have any quality problems. Second, any MODIS pixels that produced an LST error larger than 1.5 K were eliminated according to the "QC" layer. Since uncertainties may be reduced by the aggregation process, the accuracy of the aggregated MODIS LST should be better than the accuracy of the original 1.0-km MODIS LST (i.e., better than 1.5 K). Third, when aggregating the MODIS pixels into the AIRS pixel scale, there should be no invalid MODIS pixels inside the AIRS footprint and the standard error of the MODIS pixels should be < 2.0 K (to retain the homogeneity of the validation pixels). Fourth, only pixels with an observation angle of $< 20°$ from nadir were selected because the coefficients acquired in Table 1 are only applicable for nadir observations. Note that the thresholds used in the third and fourth restrictions were chosen to balance the quantity and quality of the intercomparison pixel pairs. In this study, considering the fact that intercomparison was only performed if all MODIS pixels within one AIRS pixel have the uncertainty of LST about 1.5 K, consequently, a standard error of 2.0 K for all MODIS-derived LSTs within one AIRS pixel was chosen to guarantee the relatively homogeneous pixels in LST, and also to minimize the impact

of spatial overlap error between aggregated MODIS pixels and AIRS pixels in the LST comparison. Moreover, both MODIS and AIRS have large viewing angles—up to about 50°. However, the coefficients listed in Table 1 were obtained from simulated data at the nadir. As there are very limited MODIS and AIRS pixel pairs available at the nadir, according to previous studies (Becker and Li, 1990; Sobrino et al., 1994; Wan and Dozier, 1996), the coefficients in the SW-like equation [Eq. (14)] derived for nadir views can still be used without introducing significant error to viewing angles < 20°; a viewing angle threshold of 20° was chosen to not only increase the total number of inter-comparison pixel pairs, but also minimize the error introduced by a larger viewing angle.

In this study, Australia was chosen as a study area because it has a variety of land surface coverages and many cloudless days. Moreover, it has a relatively flat terrain, which can help to further suppress LST mismatches caused by instrumental observation angles. Because AIRS and MODIS are on board the same satellite platform (AQUA) and observe the same land surface patch within about 5 min, it was possible to preclude the possibility of LST mismatches associated with observation time. At last, 20 appropriate images were obtained from May 2018—10 during the day and 10 at night (Fig. 17a); additionally, 21 appropriate images were obtained from September 2018—nine during the day and 12 at night (Fig. 17b).

Since individual validation image pairs have fewer pixels because of the four restrictions placed on them, the observations acquired in the same month were merged as one image for each of these two months. The daytime and nighttime observations were processed separately from the statistics of the retrieval residuals. Compared with the MODIS LST product, the LST could be retrieved with an accuracy of < 1.3 K for May (Fig. 18a and b) and < 1.7 K for September (Fig. 18c and d). The biases indicated that our results overestimated the LST compared with the MODIS LST product. The LST retrievals at night had an accuracy of about 1.0 K compared with MODIS LST product and were always better than those from during the day. One reason for this result is that the LST was closer to the effective mean atmospheric temperature for nighttime, indicating that the errors resulting from the linearization of the Planck function in Eq. (14) were smaller than those for the daytime. Alternatively, this result could be attributed to the fact that larger errors, due to the replacement of Δ in Eq. (9), were introduced to the retrieved T_{gi} for daytime observations because the LST during the day is usually higher than that at night. Another possible reason is that the TIR radiance of the land surface is more homogenous at night. In this case, errors owing to the process of aggregating MODIS pixels to AIRS pixel scales should be smaller than those of the more heterogenous land surfaces found in daytime observations. Additionally, scatter plots showing the MODIS LST and the LST retrieval errors demonstrate that LST was overestimated to a greater extent for daytime than for nighttime observations (Fig. 19). More pixels were retrieved with discrepancies larger than 2.0 K from MODIS LST product as the LST approached 320 K.

6. Conclusions

Prior works have documented that the SW and TES algorithms are the two most widely used LST retrieval methods. However, the SW method requires accurate LSE information and the TES method requires accurate atmospheric correction. In this study, a procedure was proposed to find a new channel configuration in the TIR region, based on which ground brightness temperatures could be retrieved accurately by using a method similar to the SW method [Eq. (14)]. Subsequently, the TES algorithm could be used to retrieve the LST without using additional atmosphere and LSE information. Finally, the proposed method and the suggested channel configuration were applied to the AIRS hyper-spectral radiance and validated by comparison with the MODIS LST product.

Results showed that the three ground brightness temperatures corresponding to 8.6 μm, 9.0 μm, and 10.4 μm could be acquired at an accuracy of about 0.65 K using the channel pairs of 8.6 μm and 12.5 μm, 9.0 μm and 12.5 μm, and 10.4 μm and 11.3 μm (width of 0.1 μm), respectively. The LST could be retrieved at an accuracy of within about 0.9 K using this TIR channel configuration. Sensitivity analyses indicated that the proposed method was not sensitive to channel FWHM and atmospheric downwelling radiance, but was sensitive to channel-center shifts and channel noise. When the channel centers shifted by −0.1 μm and − 0.2 μm, the LST retrieval accuracy dropped to 1.5 K and 1.4 K, respectively. As the channel centers shifted to longer wavelengths, the LST retrieval accuracy dropped as well—to 1.1 K and 1.0 K with channel-center shifts of 0.1 μm and 0.2 μm, respectively. Moreover, when random noise was added to the channel brightness temperatures, LST retrieval accuracy decreased from 0.97 K to 1.43 K, along with an increase in channel noise from 0.1 K to 0.3 K. All these results indicate that the location of the channel center and channel noise must both be well controlled for good LST retrieval results.

In addition to analysis using a simulation dataset, the proposed method was also applied to real AIRS images. The retrieved LST was compared with the aggregated MODIS LST product, showing that the discrepancies between the retrieved result and the MODIS product were better for nighttime observations than for daytime observations, with LST retrieval RMSE of about 1.0 K and 1.6 K, respectively. Note that these discrepancies not only included the mismatch in retrieval methods, but also included the mismatch in observation time and angles. Additionally, when considering that the MODIS LST product itself

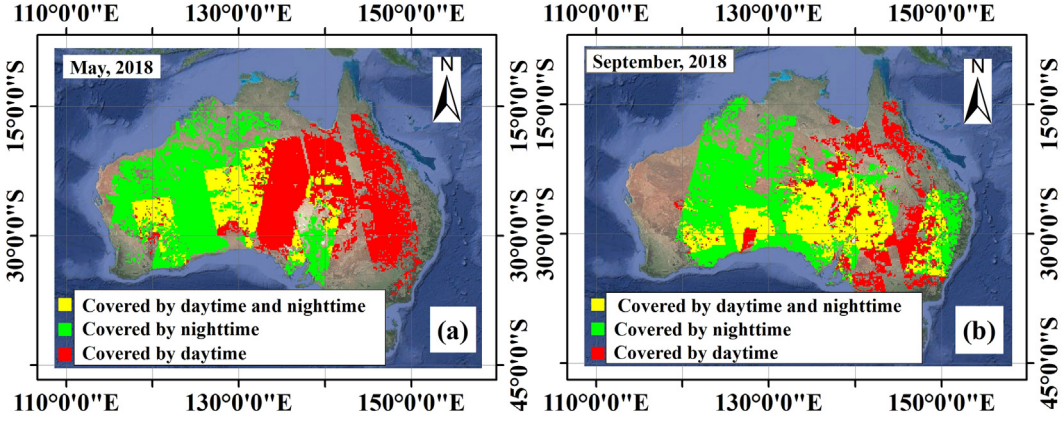

Fig. 17. The validation pixels collected in Australia and acquired in (a) May 2018, and (b) September 2018. Yellow indicates that the pixels are covered by both daytime and nighttime observations, green indicates the pixels are only covered by nighttime observations, and red indicates the pixels are only covered by daytime observations. (For interpretation of the references to color in this figure legend, the reader is referred to the web version of this article.)

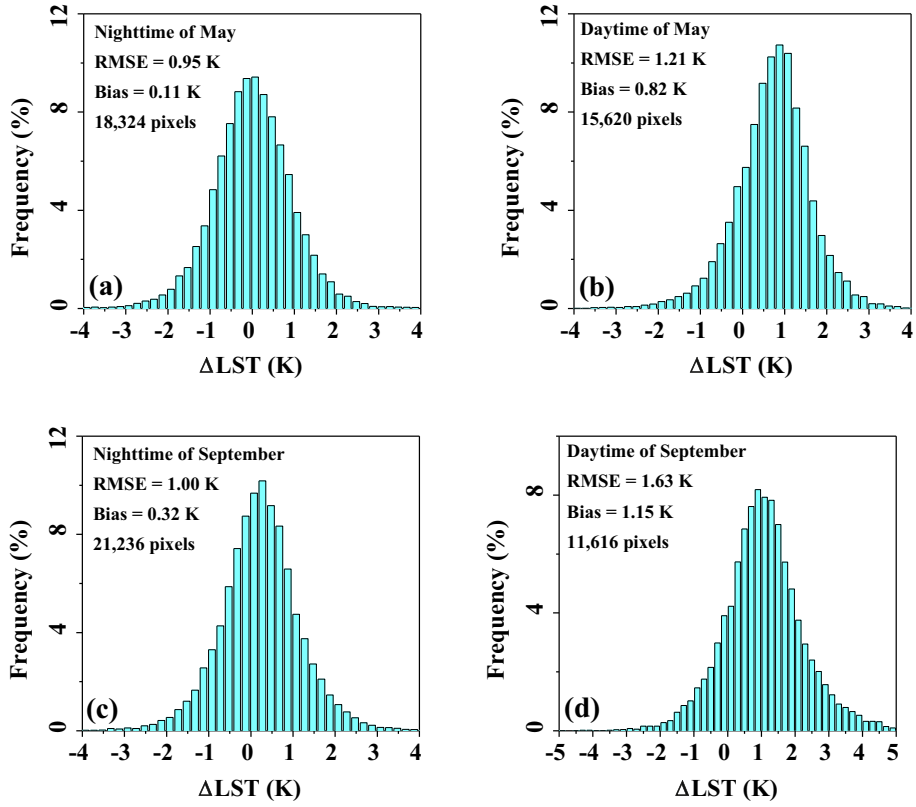

Fig. 18. Residual histograms of retrieved LST for observations of Australia acquired (a) at night in May 2018; (b) during the day in May 2018; (c) at night in September 2018; and (d) during the day in September 2018.

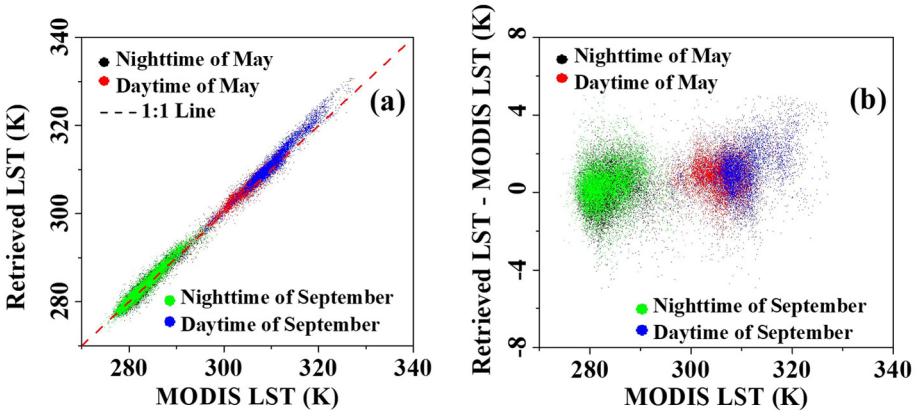

Fig. 19. (a) Scatter plot comparing the LSTs retrieved from AIRS using our proposed method and aggregated from the MODIS LST product. (b) Scatter plot of the LST difference (LST retrieved from AIRS - LST aggregated from MODIS LST product) versus the LST aggregated from the MODIS LST product.

contains an uncertainty of approximately 1.5 K, it is reasonable to conclude that the proposed method can be used to achieve LST retrievals that coincide with the MODIS products.

Our findings indicate that the proposed method could be used to retrieve LST with high accuracy, based on the suggested TIR channel configuration. In comparison with the traditional SW and TES algorithms, the proposed method requires neither accurate LSE information nor precise atmospheric correction. However, there are presently no TIR sensors with such a channel configuration. Therefore, the method has only been verified based on simulated channel filter functions. It is planned to collect and combine actual channel filter functions from several operational TIR sensors in the future in order to generate a more practical simulation dataset, based on which the proposed method will be further evaluated. Additionally, the coefficients in Eq. (14) were fixed as constants in this study; the retrieval accuracy for ground brightness temperatures may improve if they are considered as a function of atmospheric water vaper content, similar to the improvement made to the SW method. This is another aspect of future studies.

Acknowledgements

This work was supported by the China Scholarship Council (CSC). The authors would like to thank the AIRS and MODIS Science teams at NASA for providing the satellite observation data. Special thanks are due to the anonymous reviewers for their valuable comments, which have been very helpful in improving the quality of this manuscript.

References

Anderson, M.C., Norman, J.M., Kustas, W.P., Houborg, R., Starks, P.J., Agam, N., 2008. A thermal-based remote sensing technique for routine mapping of land-surface carbon, water and energy fluxes from field to regional scales. Remote Sens. Environ. 112, 4227–4241.

Becker, F., 1987. The impact of spectral emissivity on the measurement of land surface-temperature from a satellite. Int. J. Remote Sens. 8, 1509–1522.

Becker, F., Li, Z.-L., 1990. Towards a local split window method over land surfaces. Int. J. Remote Sens. 11, 369–393.

Berk, A., Anderson, G.P., Acharya, P.K., Bernstein, L.S., Muratov, L., Lee, J., Fox, M., Adler-Golden, S.M., Chetwynd, J.H., Hoke, M.L., Lockwood, R.B., Cooley, T.W., Gardner, J.A., 2005. MODTRAN5: a reformulated atmospheric band model with auxiliary species and practical multiple scattering options. Multispectral and Hyperspectral Remote Sensing Instruments and Applications Ii 5655, 88–95.

Chen, Y., Duan, S.-B., Ren, H., Labed, J., Li, Z.-L., 2017. Algorithm development for land surface temperature retrieval: application to Chinese Gaofen-5 data. Remote Sens. 9, 1–19.

Choudhury, B.J., Schmugge, T.J., Chang, A., Newton, R.W., 1979. Effect of surface roughness on the microwave emission from soils. J. Geophys. Res. 84, 5699–5706.

Choudhury, B.J., Schmugge, T.J., Mo, T., 1982. A parameterization of effective soil temperature for microwave emission. J. Geophys. Res. 87, 1301–1304.

Coll, C., Caselles, V., 1997. A split-window algorithm for land surface temperature from advanced very high resolution radiometer data: validation and algorithm comparison. J. Geophys. Res.-Atmos. 102, 16697–16713.

Coll, C., Caselles, V., Sobrino, J.A., Valor, E., 1994. On the atmospheric dependence of the split-window equation for land surface temperature. Int. J. Remote Sens. 15, 105–122.

Dash, P., Göttsche, F.-M., Olesen, F.-S., Fischer, H., 2001. Retrieval of land surface temperature and emissivity from satellite data: physics, theoretical limitations and current methods. J. Indian Soc. Remote. 29, 23–30.

Dash, P., Göttsche, F.M., Olesen, F.S., Fischer, H., 2002. Land surface temperature and emissivity estimation from passive sensor data: theory and practice-current trends. Int. J. Remote Sens. 23, 2563–2594.

Du, C., Ren, H., Qin, Q., Meng, J., Zhao, S., 2015. A practical split-window algorithm for estimating land surface temperature from Landsat 8 data. Remote Sens. 7, 647–665.

Duan, S.-B., Li, Z.-L., Leng, P., 2017. A framework for the retrieval of all-weather land surface temperature at a high spatial resolution from polar-orbiting thermal infrared and passive microwave data. Remote Sens. Environ. 195, 107–117.

Galve, J.M., Coll, C., Caselles, V., Valor, E., 2008. An atmospheric radiosounding database for generating land surface temperature algorithms. IEEE Trans. Geosci. Remote Sens. 46, 1547–1557.

Gao, C., Jiang, X., Wu, H., Tang, B., Li, Z., Li, Z.-L., 2012. Comparison of land surface temperatures from MSG-2/SEVIRI and Terra/MODIS. J. Appl. Remote. Sens. 6, 1–16.

Gillespie, A., Rokugawa, S., Matsunaga, T., Cothern, J.S., Hook, S., Kahle, A.B., 1998. A temperature and emissivity separation algorithm for advanced spaceborne thermal emission and reflection radiometer (ASTER) images. IEEE Trans. Geosci. Remote Sens. 36, 1113–1126.

Gillespie, A., Rokugawa, S., Hook, S., Matsunaga, T., Kahle, A.B., 1999. Temperature/Emissivity Separation Algorithm Theoretical Basis Document, Version 2.4. NASA/GSFC, Maryland, USA, pp. 1–64.

Gustafson, W.T., Gillespie, A.R., Yamada, G.J., 2006. Revisions to the ASTER temperature/emissivity separation algorithm. In: 2nd International Symposium on Recent Advances in Quantitative Remote Sensing, Torrent (Valencia), Spain, pp. 1–7.

Harris, 2009. Atmospheric Correction Module: QUAC and FLAASH User's Guide, Version 4.7. H.G.S.S.S. Inc, Burlington, USA, pp. 1–44.

Hu, T., Liu, Q., Du, Y., Li, H., Wang, H., Cao, B., 2015. Analysis of the land surface temperature scaling problem: a case study of airborne and satellite data over the Heihe Basin. Remote Sens. 7, 6489–6509.

Jackson, R.D., Reginato, R.J., Idso, S.B., 1977. Wheat canopy temperature: a practical tool for evaluating water requirements. Water Resour. Res. 13, 651–656.

Jackson, R., Pinterjr, P., Reginato, R., 1985. Net radiation calculated from remote multispectral and ground station meteorological data. Agric. For. Meteorol. 35, 153–164.

Jimenez-Munoz, J.C., Sobrino, J.A., 2003. A generalized single-channel method for retrieving land surface temperature from remote sensing data. J. Geophys. Res.-Atmos. 108, 1–9.

Jimenez-Munoz, J.C., Sobrino, J.A., Mattar, C., Hulley, G., Gottsche, F.-M., 2014. Temperature and emissivity separation from MSG/SEVIRI data. IEEE Trans. Geosci. Remote Sens. 52, 5937–5951.

Karnieli, A., Agam, N., Pinker, R.T., Anderson, M., Imhoff, M.L., Gutman, G.G., Panov, N., Goldberg, A., 2010. Use of NDVI and land surface temperature for drought assessment: merits and limitations. J. Clim. 23, 618–633.

Li, Z.-L., Tang, R., Wan, Z., Bi, Y., Zhou, C., Tang, B., Yan, G., Zhang, X., 2009. A review of current methodologies for regional evapotranspiration estimation from remotely sensed data. Sensors (Basel) 9, 3801–3853.

Li, Z.-L., Tang, B.-H., Wu, H., Ren, H., Yan, G., Wan, Z., Trigo, I.F., Sobrino, J.A., 2013a. Satellite-derived land surface temperature: current status and perspectives. Remote Sens. Environ. 131, 14–37.

Li, Z.-L., Wu, H., Wang, N., Qiu, S., Sobrino, J.A., Wan, Z., Tang, B.-H., Yan, G., 2013b. Land surface emissivity retrieval from satellite data. Int. J. Remote Sens. 34, 3084–3127.

Liu, Z.-L., Wu, H., Tang, B.-H., Qiu, S., Li, Z.-L., 2013. Atmospheric corrections of passive microwave data for estimating land surface temperature. Opt. Express 21, 15654–15663.

McFarland, M.J., Miller, R.L., Neale, C.M.U., 1990. Land surface temperature derived from the SSM/I passive microwave brightness temperatures. IEEE Trans. Geosci. Remote Sens. 28, 839–845.

McMillin, L.M., 1975. Estimation of sea surface temperatures from two infrared window measurements with different absorption. J. Geophys. Res. 80, 5113–5117.

Moustafa, C., 2015. AIRS/Aqua L1C Infrared (IR) Resampled and Corrected Radiances V006. Goddard Earth Sciences Data and Information Services Center (GES DISC), Greenbelt, MD, USA. https://doi.org/10.5067/Aqua/AIRS/DATA101 Accessed: [Oct. 2018].

Njoku, E.G., Entekhabi, D., 1996. Passive microwave remote sensing of soil moisture. J. Hydrol. 184, 101–129.

Ottle, C., Vidalmadjar, D., 1992. Estimation of land surface-temperature with NOAA9 data. Remote Sens. Environ. 40, 27–41.

Prata, A.J., 1993. Land surface temperatures derived from the advanced very high resolution radiometer and the along-track scanning radiometer: 1. Theory. J. Geophys. Res. 98, 16689–16702.

Prata, A.J., Caselles, V., Coll, C., Sobrino, J.A., Ottlé, C., 1995. Thermal remote sensing of land surface temperature from satellites: current status and future prospects. Remote Sens. Rev. 12, 175–224.

Qian, Y.-G., Li, Z.-L., Nerry, F., 2013. Evaluation of land surface temperature and emissivities retrieved from MSG/SEVIRI data with MODIS land surface temperature and emissivity products. Int. J. Remote Sens. 34, 3140–3152.

Qin, Z., Karnieli, A., Berliner, P., 2001a. A mono-window algorithm for retrieving land surface temperature from Landsat TM data and its application to the Israel-Egypt border region. Int. J. Remote Sens. 22, 3719–3746.

Qin, Z.H., Dall'Olmo, G., Karnieli, A., Berliner, P., 2001b. Derivation of split window algorithm and its sensitivity analysis for retrieving land surface temperature from NOAA-advanced very high resolution radiometer data. J. Geophys. Res.-Atmos. 106, 22655–22670.

Ren, H., Ye, X., Liu, R., Dong, J., Qin, Q., 2018. Improving land surface temperature and emissivity retrieval from the Chinese Gaofen-5 satellite using a hybrid algorithm. IEEE Trans. Geosci. Remote Sens. 56, 1080–1090.

Running, S.W., Justice, C.O., Salomonson, V., Hall, D., Barker, J., Kaufmann, Y.J., Strahler, A.H., Huete, A.R., Muller, J.P., Vanderbilt, V., Wan, Z., Teillet, P., Carneggie, D., 1994. Terrestrial remote sensing science and algorithms planned for EOS/MODIS. Int. J. Remote Sens. 15, 3587–3620.

Sattari, F., Hashim, M., 2014. A breife review of land surface temperature retrieval methods from thermal satellite sensors. Middle East J. Sci. Res. 22, 757–768.

Schmugge, T., Hook, S.J., Coll, C., 1998. Recovering surface temperature and emissivity from thermal infrared multispectral data. Remote Sens. Environ. 65, 121–131.

Sellers, P., Hall, F., Asrar, G., Strebel, D., Murphy, R., 1988. The first ISLSCP field experiment (FIFE). Bull. Am. Meteorol. Soc. 69, 22–27.

Simmer, C., 1999. Contribution of microwave remote sensing from satellites to studies on the Earth energy budget and the hydrological cycle. Adv. Space Res. 24, 897–905.

Sobrino, J.A., Jiménez-Muñoz, J.C., 2014. Minimum configuration of thermal infrared bands for land surface temperature and emissivity estimation in the context of potential future missions. Remote Sens. Environ. 148, 158–167.

Sobrino, J., Coll, C., Caselles, V., 1991. Atmospheric correction for land surface temperature using NOAA-11 AVHRR channels 4 and 5. Remote Sens. Environ. 38, 19–34.

Sobrino, J.A., Caselles, V., Coll, C., 1993. Theoretical split-window algorithms for determining the actual surface temperature. Il Nuovo Cimento C 16, 219–236.

Sobrino, J.A., Li, Z.-L., Stoll, M.P., Becker, F., 1994. Improvements in the split-window technique for land surface temperature determination. IEEE Trans. Geosci. Remote Sens. 32, 243–253.

Sobrino, J.A., Del Frate, F., Drusch, M., Jimenez-Munoz, J.C., Manunta, P., Regan, A., 2016. Review of thermal infrared applications and requirements for future high-resolution sensors. IEEE Trans. Geosci. Remote Sens. 54, 2963–2972.

Tomlinson, C.J., Chapman, L., Thornes, J.E., Baker, C., 2011. Remote sensing land surface temperature for meteorology and climatology: a review. Meteorol. Appl. 18, 296–306.

Vining, R.C., Blad, B.L., 1992. Estimation of sensible heat flux from remotely sensed canopy temperatures. J. Geophys. Res. 97, 18951–18954.

Wan, Z., 2008. New refinements and validation of the MODIS land-surface temperature/emissivity products. Remote Sens. Environ. 112, 59–74.

Wan, Z., 2014. New refinements and validation of the collection-6 MODIS land-surface temperature/emissivity product. Remote Sens. Environ. 140, 36–45.

Wan, Z., Dozier, J., 1996. A generalized split-window algorithm for retrieving land-surface temperature from space. IEEE Trans. Geosci. Remote Sens. 34, 892–905.

Wan, Z., Li, Z.-L., 1997. A physics-based algorithm for retrieving land-surface emissivity and temperature from EOS/MODIS data. IEEE Trans. Geosci. Remote Sens. 35, 980–996.

Wan, Z., Li, Z.-L., 2008. Radiance-based validation of the V5 MODIS land-surface temperature product. Int. J. Remote Sens. 29, 5373–5395.

Wan, Z., Hook, S., Hulley, G., 2015. MYD11_L2 MODIS/Aqua Land Surface Temperature/Emissivity 5-Min L2 Swath 1km V006. NASA EOSDIS LP DAAC. https://doi.org/10.5067/MODIS/MYD11_L2.006 Accessed: [Oct. 2018].

Yu, Y., Privette, J.L., Pinheiro, A.C., 2005. Analysis of the NPOESS VIIRS land surface temperature algorithm using MODIS data. IEEE Trans. Geosci. Remote Sens. 43, 2340–2350.